

From Heterostructures to Solid-Solutions: Structural Tunability in Mixed Halide Perovskites

Donghoon Shin, Minliang Lai, Yongjin Shin, Jingshan S. Du, Liban Jibril, James M. Rondinelli, and Chad A. Mirkin*

The stability, reliability, and performance of halide-perovskite-based devices depend upon the structure, composition, and particle size of the deviceenabling materials. Indeed, the degree of ion mixing in multicomponent perovskite crystals, although challenging to control, is a key factor in determining properties. Herein, an emerging method termed evaporation-crystallization polymer pen lithography is used to synthesize and systematically study the degree of ionic mixing of Cs_{0.5}FA_{0.5}PbX₃ (FA = formamidinium; X = halide anion, ABX₃) crystals, as a function of size, temperature, and composition. These experiments have led to the discovery of a heterostructure morphology where the A-site cations, Cs and FA, are segregated into the core and edge layers, respectively. Simulation and experimental results indicate that the heterostructures form as a consequence of a combination of both differences in solubility of the two ions in solution and the enthalpic preference for Cs-FA ion segregation. This preference for segregation can be overcome to form a solid-solution by decreasing crystal size (<60 nm) or increasing temperature. Finally, these tools are utilized to identify and synthesize solid-solution nanocrystals of Cs_{0.5}FA_{0.5}Pb(Br/I)₃ that significantly suppress photoinduced anion migration compared to their bulk counterparts, offering a route to deliberately designed photostable optoelectronic materials.

D. Shin, Y. Shin, J. S. Du, L. Jibril, J. M. Rondinelli, C. A. Mirkin Department of Materials Science and Engineering Northwestern University 2220 Campus Drive, Evanston, IL 60208, USA E-mail: chadnano@northwestern.edu
D. Shin, M. Lai, Y. Shin, J. S. Du, L. Jibril, J. M. Rondinelli, C. A. Mirkin International Institute for Nanotechnology Northwestern University Evanston, IL 60208, USA M. Lai, C. A. Mirkin Department of Chemistry

Department of Chemistry Northwestern University 2145 Sheridan Road, Evanston, IL 60208, USA

The ORCID identification number(s) for the author(s) of this article can be found under https://doi.org/10.1002/adma.202205923.

© 2023 The Authors. Advanced Materials published by Wiley-VCH GmbH. This is an open access article under the terms of the Creative Commons Attribution-NonCommercial-NoDerivs License, which permits use and distribution in any medium, provided the original work is properly cited, the use is non-commercial and no modifications or adaptations are made.

DOI: 10.1002/adma.202205923

1. Introduction

Mixed-halide perovskites consisting of multiple ions at the same lattice site (ABX₃) are an emerging class of semiconductors, with potential as highperformance optoelectronic materials.[1] The promise of this class of materials derives from the fact that incorporation of multiple ions is a facile means to tune material properties such as band structure, emission and absorption efficiency, exciton binding energy, and carrier lifetime.[1] Indeed, it has been well established that mixed-cation and mixed-halide composition perovskites lead to enhanced device performance and stability.[1,2] However, simply using multiple ions during synthesis does not always lead to structures with desirable properties, due to the various degrees of ionic mixing and types of nanoscale arrangements possible in the complex perovskite.[3] Therefore, facile perovskite property tuning using stoichiometry is difficult, if not impossible, without the ability to predict the degree of ion mixing and the evolution of

the mixing ratio under application-relevant conditions. Indeed, the ability to freely tune the crystal structure and morphology of halide perovskites might enable access to both single-phase (i.e., well-mixed solid-solution) and complex multiphase structures (i.e., core–shell, Janus, and other heterostructures) on demand. [4] Technologically speaking, phase-uniformity in a solid-solution is critical in the context of perovskite solar cells and light-emitting diodes, where challenges pertaining to photoinduced or electrical bias-induced segregation often emerge. [5]

In contrast, purposefully inducing de-mixing of ions to form multiphasic crystals is a means of engineering charge-carrier concentration and dynamics, and fabricating multijunction optoelectronic devices.^[6] Traditionally, heterostructure perovskites have been prepared by epitaxial growth, ion exchange, and phase separation. However, these structures often tend to undergo phase mixing due to either spontaneous ion diffusion or ion diffusion under external stimuli (e.g., heat, light, or an electric field).^[4,6,7] It has been previously reported that such ion migration can be significantly suppressed in 2D heterostructures where the metal-halide octahedra are isolated by long-chain organic spacer cations.^[6,8] This suggests that physical





www.advmat.de

confinement can significantly modify the thermodynamics of ionic mixing. However, a strategy capable of realizing robust 3D heterostructures of ABX₃ compositions has not been established yet due to facile ion-mixing.

In view of the challenges associated with unwanted mixing or de-mixing, methods are needed to both examine the fundamental phase behavior underpinning these processes, and ultimately prepare structures that retain their morphology under device-relevant conditions. This challenge is underscored by the fact that certain compositions (especially mixed Cs-FA-based systems, where FA = formamidinium) have been reported to either mix or phase-segregate, with no clear understanding of the contributing factors. [2,3,9] This inconsistency provides fertile ground for further study, as it implies that thermodynamically stable solid-solutions and segregated phases are comparable in energy in Cs-FA mixed cation-based perovskites. Indeed, these structures may be attributed to a balance between the soft lattice which accommodates strain well to facilitate mixing, and the fact that there is a large size mismatch between the two cations ($R_{Cs} = 1.81 \text{ Å}$, $R_{FA} = 2.79 \text{ Å}$, or $(R_{\rm FA}-R_{\rm Cs})/R_{\rm Cs}=54\%)$, which creates substitutional lattice strain and a free energy penalty for mixing.[1,10] We hypothesized therefore that varying the synthetic conditions during and after crystallization would enable modulation of the magnitude of this energy barrier, yielding a strategy for controlling the resulting degree of ion mixing. The ability to directly investigate the thermodynamics of mixing and converge on a thermodynamic structure is also useful, since the thermodynamic structure will not be affected by minute variations in the free energy landscape, and therefore, should remain stable to external stimuli.[11] However, conventional methods provide neither the degree of size and composition tunability necessary to map out the phase behavior of these complex perovskite mixtures, nor the ability to study their evolution at the singleparticle level. Therefore, probing this hypothesis requires the use of an emerging method, termed evaporation crystallization polymer pen lithography (EC-PPL), which allows systematic investigation of the ion segregation behavior in mixed Cs-FA perovskites, including high mixing-ratio compositions such as Cs_{0.5}FA_{0.5}PbX₃.^[12] Collectively through this work, we provide: 1) an explanation for the microstructural origins of the segregation process and 2) method for deliberately and systematically tuning the phase morphology, thereby allowing for the rational design of targeted emissive structures on demand.

2. Results and Discussion

2.1. Lateral Heterostructures from Step-Wise Nucleation and Growth

As an initial step toward investigating crystallite size effects, the ion segregation behaviors of microcrystals were investigated. A bulk solution growth method was developed involving deposition of the constituent perovskite ions and solvent onto a wafer followed by unconfined microcrystal growth during solvent evaporation. Modifying the ratio of constituent ions enables an investigation of the effect of precursor stoichiometry on the morphology and photoluminescence (PL) of the resulting

Cs_{1-x}FA_xPbBr₃ perovskite microcrystals. We first investigate a single halide anion (Br) composition (Cs_{1-x}FA_xPbBr₃) to validate the hypothesis that the addition of Cs_{1-x}FA_x results in cation segregation. Next, with the incorporation of multiple different anionic halides, we studied the interaction between anion distribution and Cs_{1-x}FA_x cation segregation by incorporating ratios of anions (Cl/Br or Br/I) including $Cs_{1-x}FA_xPb(Br_v/I_{1-v})_3$. As the relative FA concentration increased, the emission peak in the PL spectra of these materials shifted toward higher wavelengths (as expected given that FAPbBr3 has a smaller bandgap than CsPbBr₃).^[13] Notably, at the composition where segregation is expected to be most pronounced (x = 0.5), two shoulders were clearly observed in the PL spectrum (Figure S1, Supporting Information). For the x = 0.5 sample, we observed that the PL emission peaks were centered at 535 and 538 nm for the center and the outer edge of the microcrystal, respectively, and a phase-boundary is optically discernible (Figure 1A). Since CsPbBr3 has a larger bandgap than FAPbBr3, these spectra indicate that Cs was concentrated in the center, and FA was at the edge. Elemental maps also revealed a lateral inhomogeneous Cs distribution with high Cs and C concentrations present at the microcrystal center and periphery, respectively (Figure 1B). As the Br:Pb ratio is stable around 3:1 in both the center and edge regions (Figure S2, Supporting Information), the decreasing Cs:Pb ratio suggests that the FA ions are concentrated at the edges. With regard to crystal morphology, the edge of the crystal is slightly higher than the center, as evidenced by atomic force microscopy (AFM) (Figure S3, Supporting Information).

The system was further probed by incorporating a secondary anion to investigate whether the anion distribution would be modified due to the cation segregation. Since the perovskite bandgap is sensitive to halide anion stoichiometry, the halide segregation and Cs-FA cation segregation can be visually resolved via PL measurements. When a structure with a 1:1 mixture of both cations and anions, Cs_{0.5}FA_{0.5}Pb(Cl_{0.5}Br_{0.5})₃, was generated, unique PL emission peaks were observed in the center (450 nm) and outer edge (500 nm), respectively, as resolved by multichannel confocal imaging (Figure 1C,D). The large difference in emission wavelength was a consequence of anion segregation, which resulted in a Cl-rich center and a Br-rich edge. X-ray diffraction (XRD) confirmed the existence of these two phases in the $Cs_{0.5}FA_{0.5}Pb(Cl_{0.5}Br_{0.5})_3$ crystals (Figure S4, Supporting Information). In contrast, in microcrystals where a single cation is used, the Cl and Br anions were well-mixed throughout (CsPb(Cl_{0.5}Br_{0.5})₃ and FAPb(Cl_{0.5}Br_{0.5})₃), implying that anion segregation in this system is dependent on Cs-FA segregation (Figure S5, Supporting Information). Since the A-site cations do not substantially alter the bandgaps of these materials (as also seen in Figure 1A), the PL peak-shifts can be used to track and interpret the local anion concentrations.[14] From the PL and energy-dispersive spectroscopy (EDS) data, one can conclude that these two cation systems are lateral heterostructures with compositionally well-defined center and outer regions. Electron microscopy data are also consistent with this conclusion (vide infra). In order to understand how such lateral heterostructures form, the growth of Cs_{0.5}FA_{0.5}Pb(Cl_{1-v}Br_v)₃ was monitored during synthesis via optical/fluorescence microscopy (Text S1; Figures S6 and S7,

15214095, 2023, 11, Downloaded from https://onlinelibrary.wiley.com/doi/10.1002/adma.202205923 by Northwestern University Libraries, Wiley Online Library on [05/05/2023]. See the Terms and Conditions

ons) on Wiley Online Library for rules of use; OA articles are governed by the applicable Creative Commons

www.advmat.de

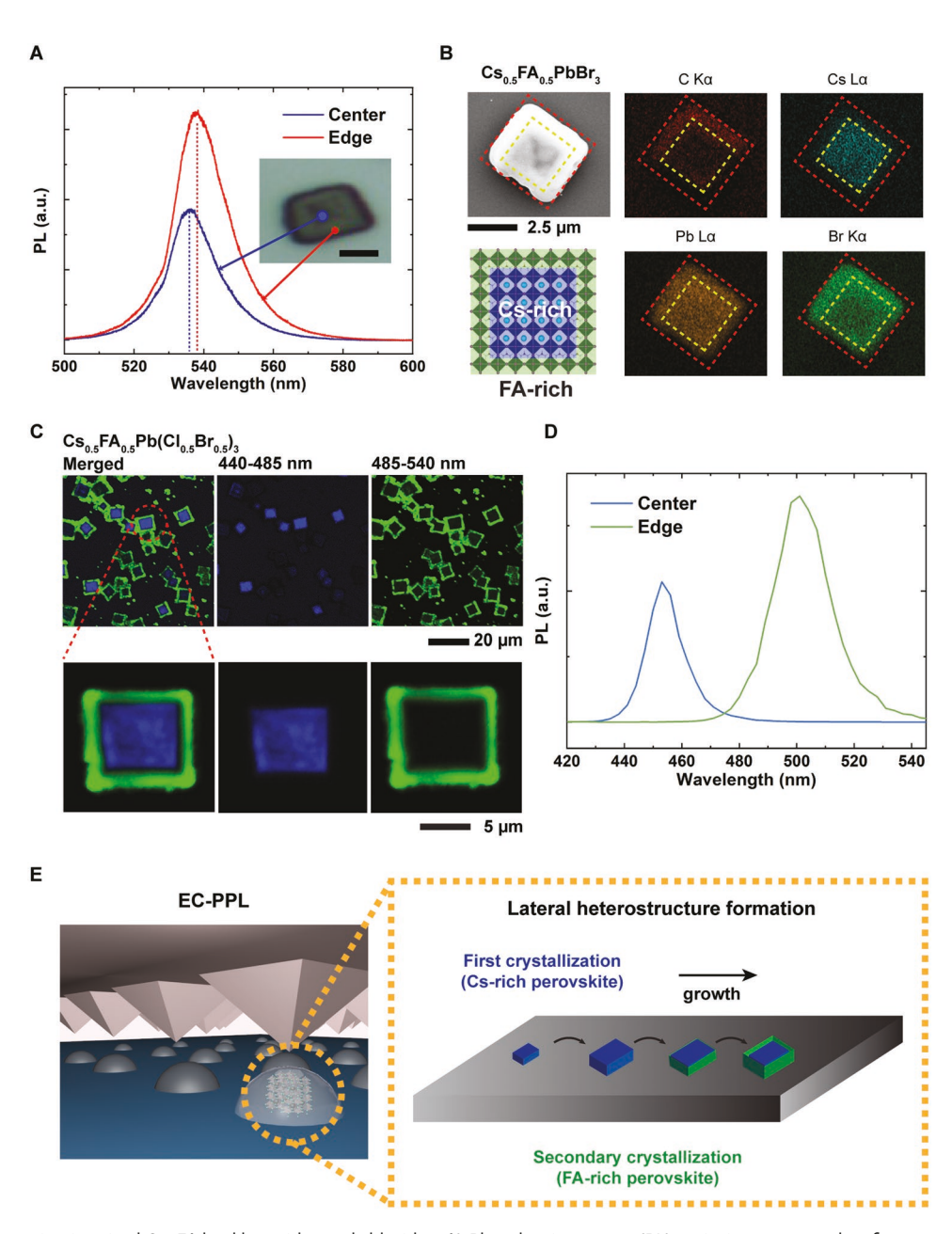


Figure 1. Ion segregation in mixed Cs-FA lead bromides and chlorides. A) Photoluminescence (PL) emission spectra taken from two different positions on a heterostructure Cs_{0.5}FA_{0.5}PbBr₃ crystal (laser excitation: 405 nm). The PL peaks from the center and edge are at 535 and 538 nm, respectively. Inset: an optical image of the crystal. Scale bar: 5 μm. B) Scanning electron microscopy (SEM) (upper left) and EDS elemental maps (right two columns) of a bulk Cs_{0.5}FA_{0.5}PbBr₃ crystal. Schematic illustrating the observed lateral heterostructure morphology consisting of a Cs-rich phase at the center and a FA-rich phase at the edge (lower left). The red and yellow dashed lines in the EDS images outline the edge and center, respectively. C) Confocal images of micron-scale mixed perovskite $Cs_{0.5}FA_{0.5}Pb(Cl_{0.5}Br_{0.5})_3$ crystals synthesized using a solution-based growth method. Different areas of the crystals emitted PL at different wavelengths. Left column: merged channels, middle column: blue channel (440-485 nm), right column: green channel (485-540 nm). D) PL spectra from the center and the edge regions of a crystal. E) Schematic illustration of EC-PPL (left) and heterostructure formation (right) for $Cs_{0.5}FA_{0.5}Pb(Cl_{1-\nu}Br_{\nu})_3$ that relies on a two-step growth process.

Supporting Information). In situ observation of the crystallization process reveals that the synthesis proceeds in two steps, beginning with the nucleation and growth of a Cs-Cl-rich perovskite phase, identified by its characteristic blue PL emission. Next, the surface of the Cs-Cl-rich perovskite acts as a heterogeneous nucleation site for the FA-Br-rich perovskite phase to form. The origin of this multistep crystallization process is the difference in solubility of the ions, as FA has a higher solubility than Cs in the solvent mixture. This discrepancy leads to sequential crystallization as opposed to simultaneous saturation (Cs-rich then FA-rich). To achieve the degree of size and composition tunability necessary, we employed a recently developed EC-PPL technique.[12] EC-PPL involves deposition of a small volume of solution upon a surface from an ink precursor;



www.advmat.de

in this scheme, the homogeneity of the mixed solution-phase droplet guarantees that all of the ion constituents participate in the eventual crystallization process. This method of incorporating diverse ions in an individual crystal facilitates the synthesis and study of complex perovskites (Figure 1E).

2.2. A Size-Dependent Morphology Transition from Lateral Heterostructure to Solid-Solution

EC-PPL permits the material-general synthesis of combinatorial arrays of the crystals on a substrate, consisting of size gradients over the micron to nanometer length scales, allowing for correlative experiments at the single-particle level (Figure 2A and Figure S8, Supporting Information).^[12] Particle lateral sizes were defined as the square root of the projected areas from the top-down using SEM or AFM images. As-synthesized Cs_{0.5}FA_{0.5} Pb(Cl_{0.5}Br_{0.5})₃ crystals ($\approx 2 \mu m$) from EC-PPL show a clear heterostructure morphology (Figure 2B). The observed PL is persistent, and the emission spectra of the crystals do not significantly change, even after 120 days under ambient conditions. This observation supports the notion that these heterostructure crystals (≈2 µm) are stable at room temperature without significant ion-migration that results in compositional changes (Figure S9, Supporting Information). Importantly, as the size of Cs_{0.5}FA_{0.5}Pb(Cl_{0.5}Br_{0.5})₃ crystals decreased, a PL emission transition was observed (Figure 2C,D) and was correlated with their morphology. For the crystals in this array (≈500 nm in size), two PL peaks were observed (461 and 483 nm), implying that two ion-segregated phases are present in individual particles. However, these peaks were either slightly red- or blue-shifted compared to those of the larger microcrystal heterostructures (450 and 500 nm in Figure 1D, respectively), likely because the degree of ion mixing increases with decreasing size. Remarkably, as the crystallite size decreased to ≈60 nm, a single PL emission peak centered at 474 nm was observed (Figure 2D), suggesting a gradual transition in morphology from the heterostructure to a well-mixed solid-solution (Figure S10, Supporting Information). In contrast, single-cation arrays from CsPb(Cl_{0.5}Br_{0.5})₃ or FAPb(Cl_{0.5}Br_{0.5})₃ particles synthesized by EC-PPL exhibit single peaks in their emission spectra for all particle sizes studied, and the observed PL peak wavelengths match reported values (Figure S11, Supporting Information).^[15] Note that in these experiments, given that the entire nanocrystal was excited, it was difficult to probe the local PL emission from the centers and edges of the nanocrystals, as the particles were smaller than the resolution of the confocal microscope and the size of the laser spot.

Transmission electron microscopy (TEM) and selected-area electron diffraction were used to determine whether structural differences arise between the heterostructure and the solid-solution phases, made possible by synthesizing crystals via EC-PPL directly on a TEM grid (Figure 2E). The crystalline structure of regions near the edges and centers of the larger heterostructure $Cs_{0.5}FA_{0.5}Pb(Cl_{0.5}Br_{0.5})_3$ crystals were clearly visible, with unique diffraction patterns (Figure 2F and Figure S12, Supporting Information). Interestingly, for the smaller 60 nm particles, high-resolution TEM (HRTEM) images show that the lattice spacing is not uniformly homogeneous

(Figure 2G,H). This inhomogeneity was distinguishable by the crystal contrast, which changed over time during extended electron dosing (i.e., the organic component of the crystal may be damaged by the beam).[3] The local phase difference observed by fast Fourier transform (FFT) may indicate that Cs and FA ions were not completely mixed at the individual ion level (Figures S13 and S14, Supporting Information). However, the crystals as a whole display a single diffraction pattern, providing evidence for a global solid-solution morphology as opposed to two superimposed yet distinct phases (Figure 2H). The microscopic origin of the obtained patterns (Figure S15, Supporting Information) was investigated using density-functional theory (DFT) simulations discussed below. The diffraction data are consistent with a global orthorhombic or tetragonal-like structure (the two are difficult to distinguish experimentally in this system), although the Goldschmidt tolerance factor suggests a cubic perovskite would be expected (≈0.94, calculated from the end members CsPbCl3 and FAPbBr3, Figure S16, Supporting Information). This result reflects the importance of cation-cation interactions in dictating the microscopic crystal arrangement.

2.3. Thermodynamics of Heterostructure and Solid-Solution Formation

Density functional theory (DFT) calculations were employed to understand the thermodynamics governing the cation segregation observed in the $Cs_{1-x}FA_xPbX_3$ $0 \le x \le 1$, X = Cl, Br, I) perovskites. The most notable features we found among all surveyed cation arrangements on the A-site are positive formation energies (**Figure 3**A; $\Delta E > 0$ at 0 K). This trend indicates a persistent energetic preference toward cation segregation in Cs_{1-x}FA_xPbX₃ at the bulk level (Text S2 and Figure S17, Supporting Information). This prediction agrees with the segregation experimentally observed in the microcrystals (Figure 2B,D). In addition, the formation energy is significantly larger at x = 0.5 compared to other compositions, and at x = 0.75 there was a considerable variation in the formation energy depending on the cation arrangement (Figure 3B). We found the formation energy is sensitive to the shape and size of the A-site cage formed by the surrounding atoms; indeed, the geometric misfit-strain associated with placing relatively large FA molecules into a smaller A-site cage increases the formation energy. The three representative cation arrangements at x = 0.5 have significantly higher formation energies than the pure separated phases, which suggests that segregation may also be favored in the Cs_{1-x}FA_xPbX₃ microcrystals as observed experimentally. Another notable feature is the asymmetric energy penalty as a function of composition; mixing FA in Cs-rich regions (x = 0.75) is energetically easier than mixing Cs in FA-rich regions (x = 0.25). This may be because the Cs-rich composition exhibits an orthorhombic packing with anisotropic A-site cation pockets within which the FA molecules can more easily fit. A detailed discussion of the complex interplay of cation arrangement, structural distortion, and energetics is provided in Text S2 and Figures S18-S20, Supporting Information.

The DFT results suggest that a large enthalpy barrier (*H*) leads to the stable cation segregation observed experimentally

15214095, 2023, 11, Downloaded from https://onlinelibrary.wiley.com/doi/10.1002/adma.202205923 by Northwestern University Libraries, Wiley Online Library on [05/05/2023]. See the Terms and Conditions

) on Wiley Online Library for rules of use; OA articles are governed by the applicable Creative Commons

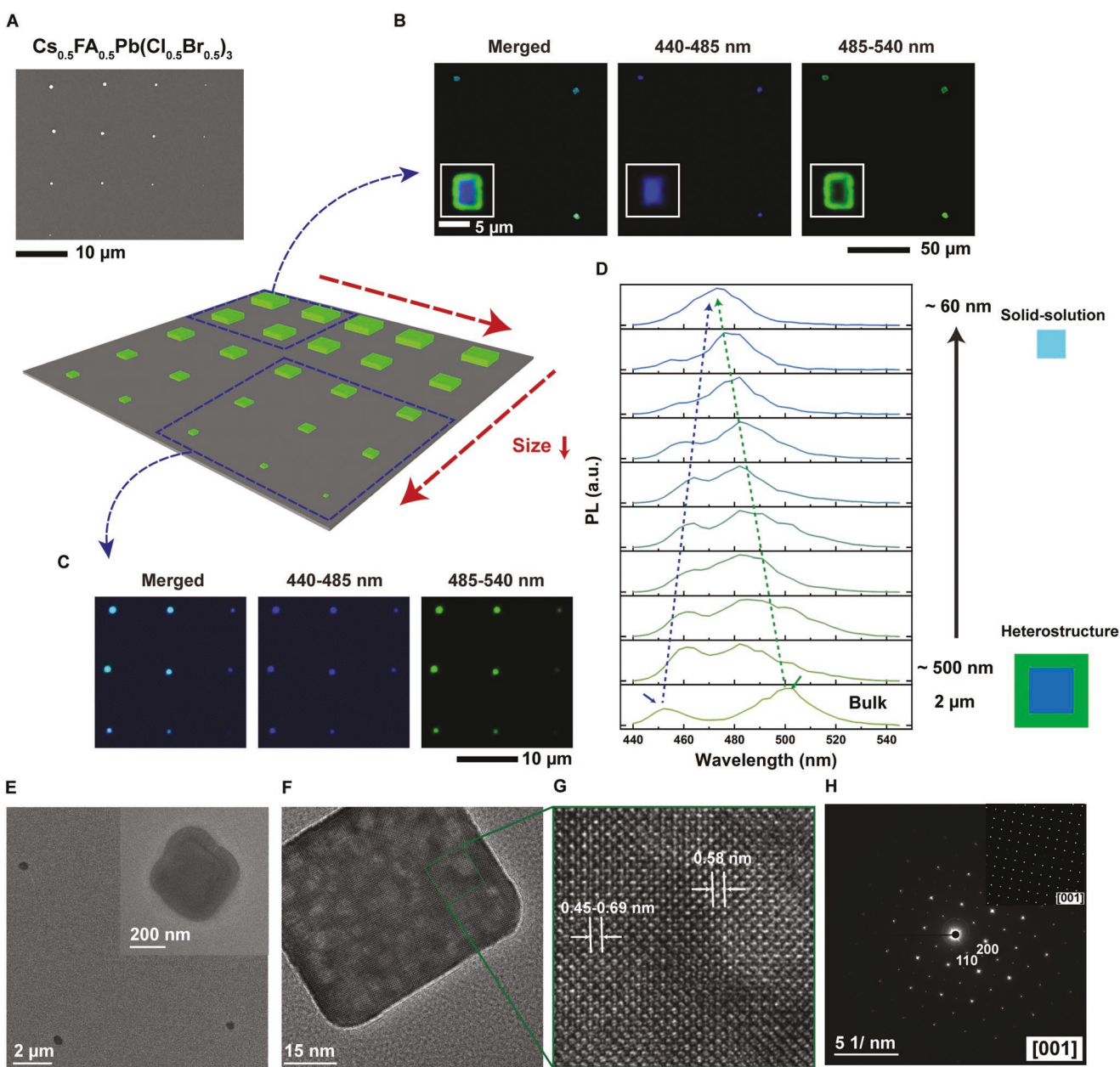


Figure 2. Size-dependent morphology, PL, and crystal structure of Cs_{0.5}FA_{0.5}Pb(Cl_{0.5}Br_{0.5})₃ nanocrystals. A) Schematic of the Cs_{0.5}FA_{0.5}Pb(Cl_{0.5}Br_{0.5})₃ crystal array via EC-PPL patterning. Top left: representative SEM image of an array of halide perovskite crystals. B,C) Multichannel confocal fluorescence images from the patterned Cs_{0.5}FA_{0.5}Pb(Cl_{0.5}Br_{0.5})₃ crystals. Left: merged channel of the arrays; center: blue channel (440–485 nm); right: green channel (485-540 nm) from heterostructure in (B) and solid-solution in panel (C). D) PL spectral evolution as a function of crystal size for the same array as in (B) and (C). The green and blue dashed arrows follow the shoulder of each PL peak. E) Low-magnification TEM image of an array of Cs_{0.5}FA_{0.5}Pb(Cl_{0.5}Br_{0.5})₃ crystals on a TEM grid, inset: high-magnification TEM image of a heterostructure. F) HRTEM image of the segregationsuppressed nanocrystal, with electron-beam damage that results in small local differences in contrast. G) Enlarged view of the green square along the [001] zone axis. The different lattices represent the locally segregated domains throughout the entire crystal. H) An experimentally obtained diffraction pattern along the [001] zone axis of the nanocrystal in G. Inset: a simulated diffraction pattern of the dispersed cation perovskite packing, $Cs_{0.5}FA_{0.5}Pb(Cl_{0.5}Br_{0.5})_3$, (along the [001] zone axis).

for larger Cs_{0.5}FA_{0.5}PbX₃ crystals. However, as temperature increases (T > 0 K), the entropic contribution (S) to the free energy of formation (G) increases, so we hypothesized that it may be possible to induce a well-mixed solid-solution in this manner (Figure 3C and Text S3, Supporting Information). Importantly, larger $Cs_{0.5}FA_{0.5}Pb(Cl_{0.5}Br_{0.5})_3$ crystals (>5 µm) were stable in heterostructure morphologies when annealed at 120 °C for extended periods (Figure S21, Supporting Information). This is because the enthalpic barrier is too large to be overcome over this size range, despite the enhanced entropic contribution to the free energy. However, in the case of single cation compositions such as CsPb(Cl_{0.5}Br_{0.5})₃, kinetic

15214095, 2023, 11, Downloaded from https://onlinelibrary.wiley.com/doi/10.1002/adma.202205923 by Northwestern University Libraries, Wiley Online Library on [05/05/2023]. See the Terms and Conditions (https://orthwestern.

conditions) on Wiley Online Library for rules of use; OA articles are governed by the applicable Creative Commons

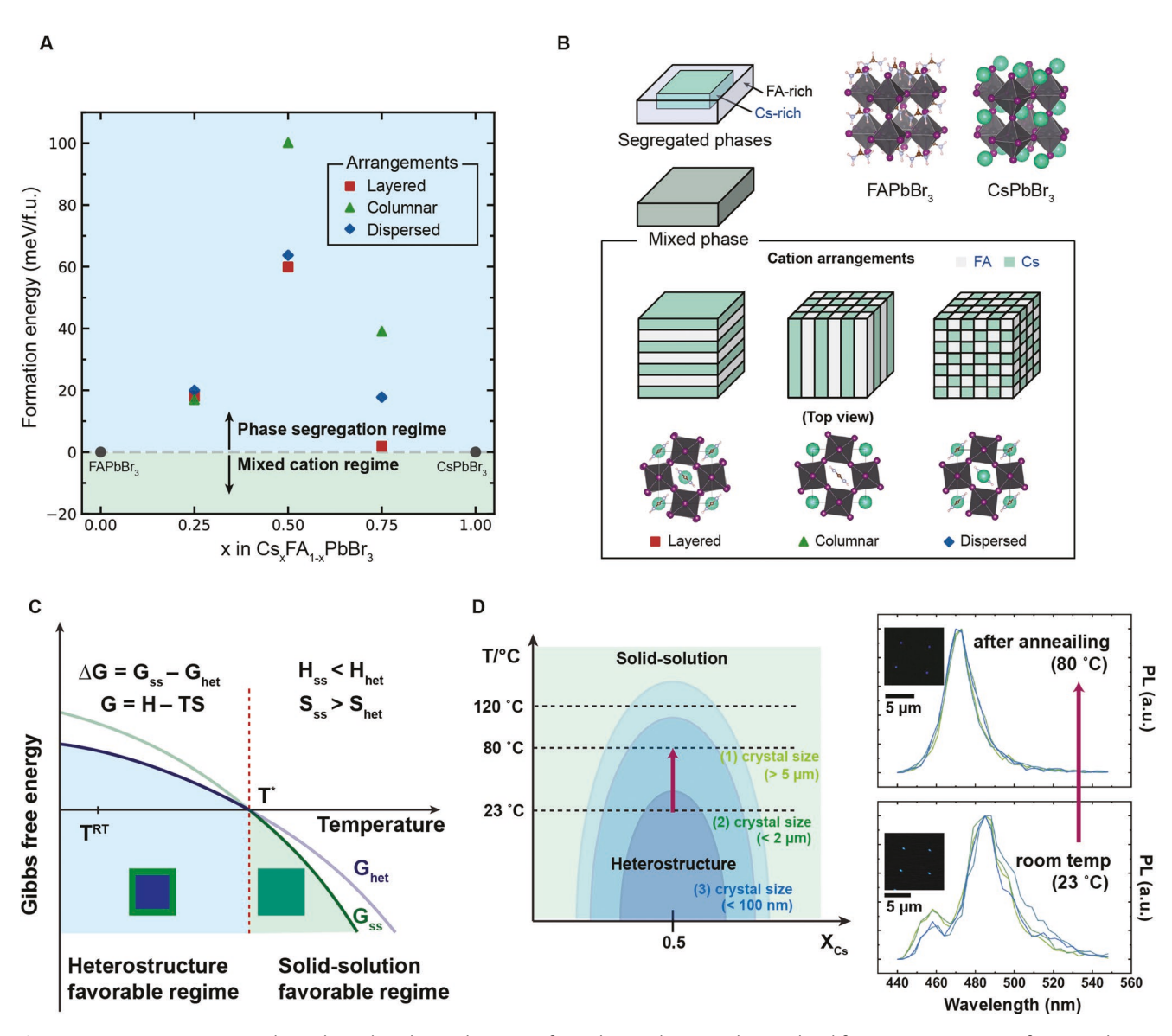


Figure 3. Cation arrangement and size-dependent thermodynamics of mixed perovskites. A) The simulated formation energy (ΔE) of Cs_vFA_{1-v}PbBr₃ as a function of FA concentration (x = 0, 0.25, 0.5, 0.75, and 1) at 0 K. The gray dashed line represents the x-axis ($\Delta E = 0$). Blue and green shades represent the phase-segregation regime and mixed regime, respectively. B) Schematics illustrating the segregated phases and mixed phase. In mixed phases, different arrangements were investigated, and energy variations occurred depending on cation arrangements as shown in (B). The layered order represents clusters of FA molecules on the same layer, and this structure is a higher-energy configuration. The columnar and the dispersed arrangements represent the intermediate and lower-energy configurations, respectively. The green, pink, and clustered spheres represent the Cs cations, halide anions, and the FA cations, respectively. C) The final structures can be classified as either entropically favorable (solid-solution) or entropically unfavorable (phase-segregated). G_{ss} and G_{hot} : Free energies of solid-solution and heterostructure. T^{RT} and T^* : Room temperature and critical temperature. D) Left: schematic of estimated miscibility gaps being suppressed as crystal size decreases. Each blue shade inward represents the immiscible regime as crystal size decreases. Right: PL spectra from ≈100 nm crystals in the array before (bottom) and after annealing (top). Red arrow indicates the annealing process. Inset: confocal images of the particles from the array before and after annealing process.

heterostructure morphologies formed for exceptionally large microcrystals (>30 μm, Figure S22, Supporting Information), but low-temperature annealing (100 °C) was sufficient to induce complete mixing. This observation corroborates the idea that the Cs-FA enthalpic barrier is the key to robust heterostructure formation.

As particle size decreases, the roles of surface and interfacial energies become more relevant to determining the thermodynamically preferred structure, and generally, these contributions favor mixing.[11a,16] Thus, for the heterostructures, we hypothesized that the immiscible region of the phase diagram would shrink with decreasing crystal size (Figure 3D). Indeed, compared to the stable larger Cs_{0.5}FA_{0.5}Pb(Cl_{0.5}Br_{0.5})₃ crystals (>5 μ m), Cs_{0.5}FA_{0.5}Pb(Cl_{0.5}Br_{0.5})₃, crystals \approx 2 μ m in size showed a transition from a heterostructure to a solid-solution morphology after thermal annealing at 120 °C (Figure S23, Supporting Information). We further observed a lower transition temperature (80 °C) for ≈100 nm edge length





www.advmat.de

 $Cs_{0.5}FA_{0.5}Pb(Cl_{0.5}Br_{0.5})_3$ crystals (Figure 3D). As for the even smaller crystals ≈ 60 nm in size, their transition temperature appears to be below room temperature (23 °C). However, the role of kinetic effects during crystallization of the smaller sized particles should not be ignored. Long-range ion transport is slow within larger crystals due to the slow diffusivity of the cations, and the smaller crystals facilitate short-range ion mixing. Indeed, given the fact that the separated two PL peaks merge to the single peak as crystal size decreases and that these structures can withstand thermal annealing, we suspect diffusion constraints are secondary to the difference in mutual solubility of the cations which drive the final morphology.

2.4. A Library of Complex Mixed-Halide Perovskites Illustrates Phase-Dependence on Size

Having evaluated the microscopic origins of the lateral heterostructure morphology and its size dependence, we hypothesized that the physical confinement enabled by EC-PPL may allow the generalization of the synthesis scheme to new precursor ions and ratios. Additionally, control over particle size serves as another facile means of tuning the particle morphology, degree of mixing, and ultimately PL. Indeed, we were successful in using EC-PPL to synthesize a library of 10 representative heterostructures and solid-solution perovskites, simply by extrapolating observations on their formation energy as well as varying halide anion concentrations and particle sizes (Figure 4A–C). By tuning anion identity or ratio, we achieved synthesis of a variety of unique heterostructures with specific center and edge PL peaks. The result was tunability of the PL peak emission centers from ≈420 to ≈700 nm. For example, we extrapolated the Cl, Br anion mixture to a Br, I mixture: $Cs_0 {}_5FA_0 {}_5Pb(Br_{1-\nu}I_{\nu})_3$. As expected, larger microcrystals form a heterostructure, but in this case with a Cs-Br-rich center and a FA-I-rich periphery. As the particle size decreased in this system, the expected solidsolution was observed optically (Figure 4D,E). Interestingly, incorporating all three anions in Cs_{0.5}FA_{0.5}(Cl_{0.42}Br_{0.42}I_{0.17})₃ led to a unique morphology consisting of a core, double lateral shell structure. According to the PL emission, the Cl anions are present in the center, with Br anions in the inner lateral shell and then I anions in the outer lateral shell; the formation energy trends suggest that the Cs:FA ratio should decrease from the core outward (Table S1, Supporting Information). However, due to increased complexity, we could not assign precise ion distributions solely from the PL data (Figure S25, Supporting Information).

2.5. Mitigation of Photoinduced Phase Segregation

Photoinduced anion segregation has proven to be a significant barrier to the practical use of mixed anion perovskite systems, because it results in device deterioration, especially in the APb(Br_{1-y}I_y)₃ (A = MA or FA) compositions where $0.2 \le y \le 0.7$ holds true. [5,18] We observed the same anion migration effect as well during photoillumination of the Cs_{0.5}FA_{0.5}Pb(Br_{1-y}I_y)₃ heterostructure crystals. Crystals were irradiated with a 473 nm

laser with a laser power of 30 mW cm⁻². When the as-synthesized crystals with an anion composition of y = 0.2 were exposed to laser excitation for several minutes, significant red-shifts in the PL peak positions were observed (Figure 4F), indicating photoinduced iodide-ion segregation occurred.[18,19] Since the laser spot size is too large to selectively illuminate either the edge or core phases of the heterostructure, it is impossible to determine whether the PL changes emerge from the diffusion across the junction or between FA-rich and Cs-rich areas. Several models have been reported to explain photoinduced anion segregation, including ones based on polaron-induced lattice strain. [5,20] In these heterostructures, it is likely that polarons form due to the incorporation of both Br and I, as well as the structurally expected interfacial strain between the FA-rich peripheral layer and the Cs-rich core, which enhances the electron-lattice coupling strength (as suggested in inset Figure 4F). The polaroninduced strain favors the formation of local iodide-ion enriched domains. Some researchers have reported that incorporating a mixture of organic and inorganic cations in the A-site (i.e., incorporating Cs into FA site) alleviates this polaron-induced phenomenon by decreasing the degree of electron-phonon coupling, which suppresses anion segregation.^[20,21] However, since highly mixed cation perovskites, $Cs_{0.5}FA_{0.5}Pb(Br_{1-\nu}I_{\nu})_3$, have yet to be studied due to their limited cation miscibility, it remains difficult to examine the polaron-induced segregation at higher mixing fractions. To investigate this, we synthesized small ion mixed particles with the same composition as the microcrystals, Cs_{0.5}FA_{0.5}Pb(Br_{0.8}I_{0.2})₃, which showed substantially improved stabilities under illumination (3-min accumulation; Figure 4G) over the heterostructure analog. This result shows that cation incorporation in the A-site can serve as a general strategy to mitigate light-induced anion segregation in mixed $Br_{\nu}/I_{1-\nu}$ crystals. Most importantly, these results highlight how rational mixing strategies enable the design of crystals that provide the best combination of stability and performance.

3. Conclusion

This work shows that bulk solution growth and EC-PPL can be used in tandem to synthesize and study libraries of new halide perovskite materials. These experiments serve as a first-step toward generating a comprehensive size- and compositiondependent phase diagram suitable for predicting whether a heterostructure or solid-solution is thermodynamically preferred. We have learned that in the mixed Cs-FA system, cation immiscibility results in separated lateral heterostructures. When multiple anions are incorporated, each anion preferentially associates with one cation over the other, which can be used to understand the relationship between crystal composition, its morphology/structure, and its characteristic PL emission. Several effective methods were introduced and developed to induce mixing in systems where two immiscible phases were present in the bulk. Generally, increasing the temperature, decreasing the crystal size (to ≈60 nm), or modifying the Cs-FA ratio (away from 1:1) are the most effective methods for inducing a structural transition from ion-segregated heterostructures to well-mixed solid-solutions. Importantly, the principles established here have led to an effective size-confinement

15214095, 2023, 11, Downloaded from https://onlinelibrary.wiley.com/doi/10.1002/adma.20220523 by Northwestern University Libraries, Wiley Online Library on [05/05/2023]. See the Terms and Conditions (https://onlinelibrary.wiley.com/doi/10.1002/adma.20220523 by Northwestern University Libraries, Wiley Online Library on [05/05/2023]. See the Terms and Conditions (https://onlinelibrary.wiley.com/doi/10.1002/adma.20220523 by Northwestern University Libraries, Wiley Online Library on [05/05/2023]. See the Terms and Conditions (https://onlinelibrary.wiley.com/doi/10.1002/adma.20220523 by Northwestern University Libraries, Wiley Online Library on [05/05/2023]. See the Terms and Conditions (https://onlinelibrary.wiley.com/doi/10.1002/adma.20220523 by Northwestern University Libraries, Wiley Online Library on [05/05/2023]. See the Terms and Conditions (https://onlinelibrary.wiley.com/doi/10.1002/adma.20220523 by Northwestern University Libraries, Wiley Online Library.

onditions) on Wiley Online Library for rules of use; OA articles are governed by the applicable Creative Commons

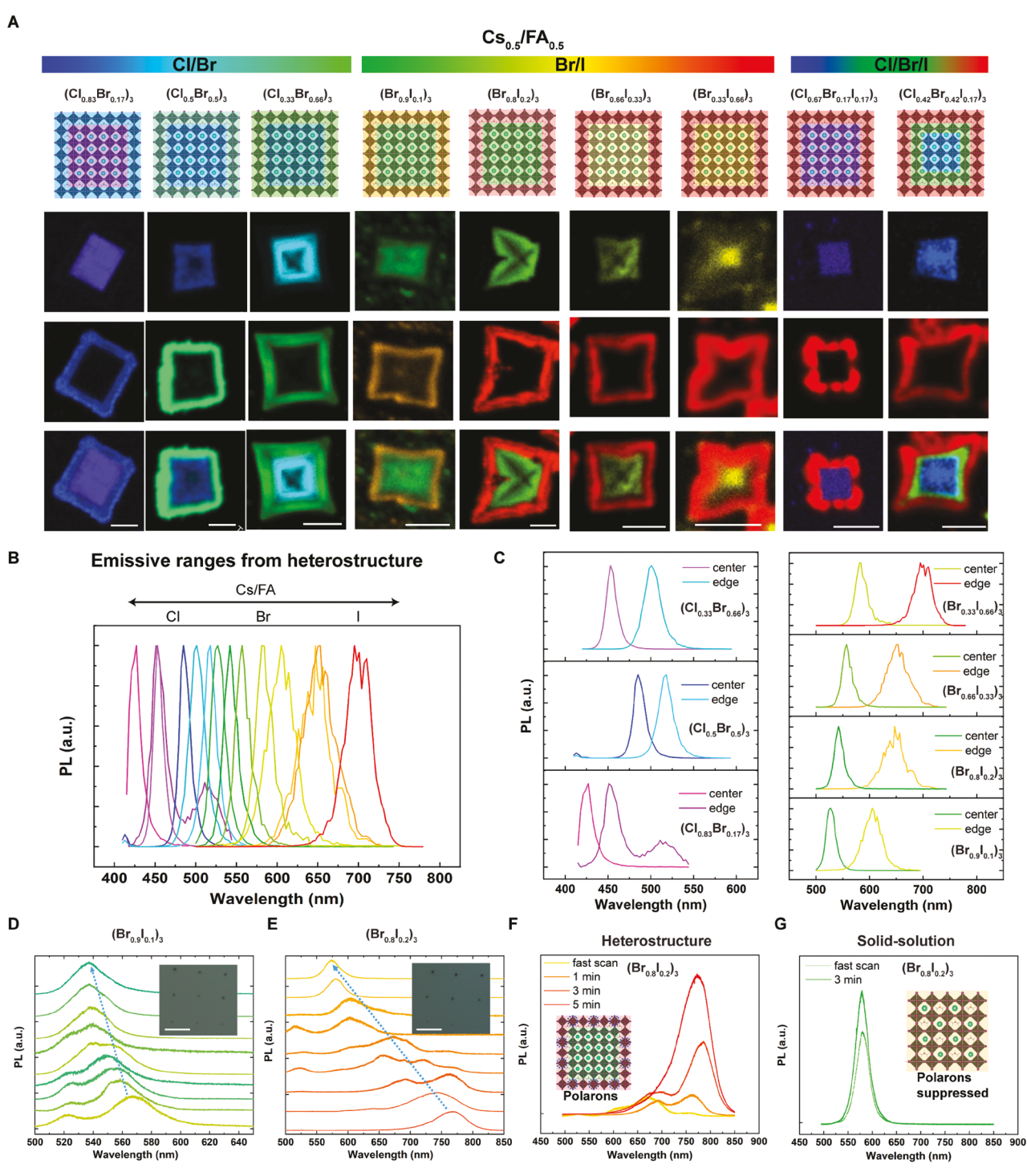


Figure 4. Heterostructure and solid-solution crystals and their stabilities under illumination. A) A library of complex halide perovskite heterostructures synthesized using EC-PPL and characterized by confocal microscopy. Top row: false-color schemes of the heterostructure with anions labeled as center, edge,; Subsequent rows: confocal images of the heterostructure library. The false colors are coded with the color of their corresponding PL peaks for the center and edge phases, respectively. Scale bars: 5 µm. B) Demonstrating the tunability of the PL of individual heterostructure crystals from the edge and center. C) From (A) and (B), composition dependence of PL spectra with; Left column: binary Cl/Br. Right column: binary Br/I. PL spectra from ternary Cl/Br/I could not be obtained due to irreversible anion migration. A representative crystal structure, $Cs_{0.5}FA_{0.5}Pb(Br_{1-\nu}I_{\nu})_3$ ($\gamma=0.1$ and 0.2), is analyzed in (D-G). D) PL evolution of Cs_{0.5}FA_{0.5}Pb(Br_{0.9}I_{0.1})₃ with varying crystal sizes from 60 nm to 1 µm. The shoulders at 520 and 568 nm merge into a single peak at 540 nm for particles \approx 60 nm in size. E) PL evolution as a function of $Cs_{0.5}FA_{0.5}Pb(Br_{0.8}I_{0.2})_3$ crystal size. The shoulders merge to a single peak at 575 nm for particles ≈60 nm in size. Insets: optical images of the array, scale bar: 5 µm. F) The changes in the PL spectra at three different time points for the $Cs_{0.5}FA_{0.5}Pb(Br_{0.8}I_{0.2})_3$ heterostructure. G) Steady-state PL spectra of the crystal $Cs_{0.5}FA_{0.5}Pb(Br_{0.8}I_{0.2})_3$. Insets: Schematics of hypothesized polaron behavior in heterostructures and solid-solutions.



www.advmat.de

strategy to suppress light-induced anion segregation in $Cs_{0.5}FA_{0.5}Pb(Br_{1-\gamma}I_{\gamma})_3$ nanocrystals. This provides a promising method for maximizing the stability of technologically relevant Br/I mixed crystals.

This work establishes a new set of tools for investigating the structure-property relationships in the vast parameter space that defines halide perovskites, where rather than exploring and studying structures through trial and error, an entire complex phase space can be mapped extensively beforehand by patterning a library of positionally encoded complex mixed perovskite crystals. Furthermore, by exploring en masse the relationship between laser exposure and crystal composition and morphology, researchers can now rapidly identify photostable structures. Similarly, if lateral heterostructures are desired for their unique properties, a persistent phase boundary which is insensitive to these same stimuli may likewise be designed. A key takeaway is that many compositions previously inaccessible due to presumed stability challenges may be worth reexploring. As such, the results reported here expand the toolkit available to researchers interested in discovering the materials necessary for generating high-performing perovskite-based optoelectronic devices.

4. Experimental Section

Synthesis of Complex Mixed-Halide Perovskite Heterostructure Microcrystals: All of the chemicals were purchased from Sigma Aldrich unless otherwise stated. For the $Cs_{0.5}FA_{0.5}Pb(Cl_{0.5}Br_{0.5})_3$ system, FABr (0.25 mmol), CsCl (0.25 mmol), PbBr₂ (0.25 mmol), and PbCl₂ (0.25 mmol) were dissolved in 10 mL of DMSO. Then, the Cs_{0.5}FA_{0.5}P $\dot{b}(Cl_{0.5}Br_{0.5})_3$ solution was drop-casted on O_2 plasma-pre-treated Si substrates. The substrates were heated at ≈120 °C for ≈10 min on a hot plate in the air. The square-shaped heterostructure microcrystals formed after the solvent fully evaporated. For the other mixed-composition perovskites (Figure 4) (i.e., $Cs_0 \,_5FA_0 \,_5PbBr_3$, $Cs_0 \,_5FA_0 \,_5Pb(Cl_0 \,_83Br_0 \,_{17})_3$, $Cs_{0.5}FA_{0.5}Pb(Cl_{0.33}Br_{0.66})_3$, $Cs_{0.5}FA_{0.5}Pb(Br_{0.9}l_{0.1})_3$, $Cs_{0.5}FA_{0.5}Pb(Br_{0.8}l_{0.2})_3$, $Cs_{0.5}FA_{0.5}Pb(Br_{0.66}I_{0.33})_3$, $Cs_{0.5}FA_{0.5}Pb(Br_{0.33}I_{0.66})_3$, $Cs_{0.5}FA_{0.5}Pb(Cl_{0.67}$ $Br_{0.17}l_{0.17})_3$, $Cs_{0.5}FA_{0.5}Pb(Cl_{0.42}Br_{0.42}l_{0.17})_3)$, the precursor solutions were prepared with the corresponding ratios of CsX, FAX, and PbX₂ (X = Cl, Br, I) dissolved in dimethyl sulfoxide (DMSO). The crystal growth process was similar to that for Cs_{0.5}FA_{0.5}Pb(Cl_{0.5}Br_{0.5})₃ above. The sizes and shapes of the centers and the peripheral layers in the heterostructures could be changed by modifying the solution evaporation rate. The overall crystal size was tuned by varying the concentration of precursors in solution and the ratio of the solvents. A smaller Cs_{0.5}FA_{0.5}Pb(Cl_{0.5}Br_{0.5})₃ heterostructure microcrystal (used for the data in Figure S23, Supporting Information) was obtained by diluting DMSO using dimethyl formamide (DMF) (DMF:DMSO in a volume ratio of 9:1 (0.05 M)). The as-synthesized crystals were annealed at different temperatures, as needed, to improve their crystallinity.

Synthesis of Complex Mixed-Halide Perovskite Arrays: Mixed-halide perovskite arrays were synthesized by EC-PPL following literature methods. [12] For consistency with the bulk heterostructure synthesis, the same inks and substrate were used. The pyramidal-shaped polymer pen arrays were fabricated following a published protocol using h-polydimethylsiloxane (h-PDMS, Gelest). [122] The pen arrays were mounted onto the XYZ-motorized piezo scanner of a desktop nanopatterning instrument (TERA-Fab M series, TERA-print, LLC). The pen array was finely leveled parallel to the substrate with two piezoactuators before patterning. The pen array was removed from the instrument, treated with O₂ plasma, and then spin-coated with the ink at a spin speed of 3000 rpm for 1 min or less depending on the type of ink precursor used. The inked pen array in the instrument was brought

in contact with the substrate for a few seconds, and then retracted from the substrate to make small nanoreactors.

The crystal size was tuned by modulating dwell time (pen in contact with the substrate for 1–10 s) and extension length (0–10 μm from a contact point against the substrate). Nanoreactors of the ink was formed on the substrate after retraction of the pen array, and these droplets were allowed to evaporate under atmospheric conditions to form individual halide perovskite nanocrystals, in line with previous nanoreactor approaches. $^{[23]}$

To achieve patterning at high-temperature, a home-built microheater, which was made up of Pt-wires 0.2 mm in diameter, was attached below the substrate. Consistent heat was applied to the substrate during the patterning. The temperature on the surface of the substrate was measured using a thermocouple probe.

Nucleation Kinetics Comparison Experiment: The time-transient nucleation of $Cs_{0.5}FA_{0.5}Pb(Cl_{0.5}Br_{0.5})_3$ was imaged using an optical microscope (Zeiss Axio Imager M2) under bright-field and fluorescence modes with a LED illuminator (X-Cite, Excelitas Tech). For the kinetic comparison between $CsPbBr_3$ and $FAPbBr_3$, similar amounts of solutions were accumulated onto the pyramidal tips of the uniform pen array by controlling the spin-coating conditions. The nucleation kinetics of $CsPbBr_3$ and $FAPbBr_3$ were compared using a CMOS camera (objective: $20\times$) equipped on the TERA-Fab M series instrument.

Structure and Morphology Characterization: The morphologies of all the crystals were imaged by scanning electron microscopy (SEM) on both a Hitachi SU8030 and a JEOL JSM-7900FLV equipped with a cold field-emission gun (cFEG) operated at 1 kV to 15 kV. Elemental distributions were confirmed using EDS silicon drift detector (X-Max^N, Oxford Instruments) equipped on a Hitachi SU8030.

TEM was performed on a JEOL ARM200CF equipped with a cFEG operated at 200 kV. Diffraction patterns were obtained from a Gatan OneView CMOS camera. All images were obtained within a few seconds after the focusing and alignment process to avoid extensive electron beam damage. Simulated electron diffraction data were generated using the SingleCrystal package (SingleCrystal and CrystalMaker Software, Ltd.) based on the simulated crystal structures from the DFT results. The structural models were constructed using the VESTA software.

The heights of the heterostructures were defined using AFM (Dimension Icon; Bruker) in tapping mode (probe $k=42~\rm N~m^{-1}$) at a scan rate between 0.10–0.20 Hz. The obtained images were analyzed using Gwyddion software.

Grazing-incidence X-ray diffraction analysis was performed using a SmartLab Rigaku X-ray operating with Cu K_{α} radiation at 40 kV and 30 mA at room temperature. The scan rate was 2 s per step with a step size of 0.02°.

Optical Characterization: Crystals that exhibited multiple PL frequencies were imaged using confocal fluorescence microscopy on a Leica SP8 Confocal (Leica Microsystem). All optical sections were acquired with an objective ($10\times/0.40$ NA air; pinhole size = 1 AU) with a high-resolution zoom at room temperature. The crystals were excited using a solid-state diode laser at 405 nm.

For the resolution-sensitive heterostructures, high-resolution photoluminescence (HRPL) was performed on a modified confocal Raman spectrometer, LabRAM HR Evolution (Horiba), with an excitation wavelength of 473 nm at room temperature.

DFT Simulation: The Vienna Ab initio Simulation Package was used to investigate the electronic structure and relative stability of the halide perovskites. [24] The calculation utilized generalized gradient approximation with the Perdew–Burke–Ernzerhof functional. Projector-augmented wave potentials were used to describe the core and valence electrons, and the plane-wave basis set employed a kinetic energy cutoff of 550 eV. [25] The tetrahedron method was used along with $5\times4\times5$ Monkhorst-Pack grids for Brillouin zone integrations and k-space sampling of the Pnma unit cell with four formula units. [26] This orthorhombic unit cell was a $\sqrt{2}\times2\times\sqrt{2}$ supercell of primitive cubic cell (containing one formula unit) and has Pnma symmetry and $a^+b^-b^-$ tilt pattern in Glazer notation. [27] This tilt pattern was applied as initial structures for all $Cs_{1-x}FA_xPbX_3$ systems. For x=0.25 and $0.75, \sqrt{2}\times\sqrt{2}\times1$



www.advmat.de

supercell of the orthorhombic cell was constructed (equivalent to $2\times2\times2$ supercell of primitive cubic cell), and $4\times4\times4$ k-point grid was used. The cell volume and atomic positions were relaxed until the forces on each atom were less than 0.03 eV Å $^{-1}$. The formation energy (ΔE) of $Cs_{1\rightarrow x}FA_xPbX_3$ was calculated based on the following formula: ΔE ($Cs_{1\rightarrow x}FA_xPbX_3$) = E ($Cs_{1\rightarrow x}FA_xPbX_3$) – $xE(FAPbX_3)$ – $(1-x)(CsPbX_3)$. A full list of core and valence electrons used for the calculations and cation arrangements of each mixing composition are provided in the Supporting Information.

Supporting Information

Supporting Information is available from the Wiley Online Library or from the author.

Acknowledgements

The project described was supported by the Sherman Fairchild Foundation, Inc. and the Materials Research Science and Engineering Center through the National Science Foundation award DMR-1720139. DFT calculations were performed using the Extreme Science and Engineering Discovery Environment (XSEDE) supported by National Science Foundation award ACI-1548562. Leica SP8 confocal microscopy was performed at the Biological Imaging Facility at Northwestern University supported by the Chemistry for Life Processes Institute, the NU Office for Research, the Department of Molecular Biosciences and the Rice Foundation. This work also made use of the Jerome B. Cohen X-Ray Diffraction Facility supported by the Materials Research Science and Engineering Center (MRSEC) program of the National Science Foundation (DMR-1720139), NUANCE Center, NUFAB, and SHyNE Resource instrumentation and services at Northwestern University which have received support from the SHyNE Resource (NSF ECCS-2025633), the IIN, and Northwestern's MRSEC program (NSF DMR-1720139).

Conflict of Interest

The authors declare no conflict of interest.

Author Contributions

D.S. and M.L. contributed equally to this work. C.A.M. supervised the research. D.S. and M.L. developed and conducted the synthesis. D.S. and M.L. performed microscopy and PL experiments. Y.S. performed DFT calculation. All authors contributed to data analysis and manuscript preparation with C.A.M. assuming the lead. The authors thank Dr. S. H. Petrosko (Northwestern University) for providing editorial input.

Data Availability Statement

The data that support the findings of this study are available from the corresponding author upon reasonable request.

Keywords

halide perovskites, nanolithography, robust heterostructures, solidsolutions, structural tunability, suppressed photoinduced phase segregations

> Received: June 29, 2022 Revised: September 24, 2022 Published online: February 5, 2023

- a) D. P. McMeekin, G. Sadoughi, W. Rehman, G. E. Eperon, M. Saliba, M. T. Horantner, A. Haghighirad, N. Sakai, L. Korte, B. Rech, M. B. Johnston, L. M. Herz, H. J. Snaith, Science 2016, 351, 151; b) F. Xu, T. Zhang, G. Li, Y. Zhao, J. Mater. Chem. A 2017, 5, 11450.
- [2] a) M. Zhang, H. Yu, M. Lyu, Q. Wang, J. H. Yun, L. Wang, Chem. Commun. 2014, 50, 11727; b) W. Rehman, D. P. McMeekin, J. B. Patel, R. L. Milot, M. B. Johnston, H. J. Snaith, L. M. Herz, Energy Environ. Sci. 2017, 10, 361; c) Y. Fu, X. Jiang, X. Li, B. Traore, I. Spanopoulos, C. Katan, J. Even, M. G. Kanatzidis, E. Harel, J. Am. Chem. Soc. 2020, 142, 4008; d) G. Tong, H. Li, G. Li, T. Zhang, C. Li, L. Yu, J. Xu, Y. Jiang, Y. Shi, K. Chen, Nano Energy 2018, 48, 536; e) X. Zhang, H. Liu, W. Wang, J. Zhang, B. Xu, K. L. Karen, Y. Zheng, S. Liu, S. Chen, K. Wang, X. W. Sun, Adv. Mater. 2017, 29, 1606405; f) F. Ruf, M. F. Aygüler, N. Giesbrecht, B. Rendenbach, A. Magin, P. Docampo, H. Kalt, M. Hetterich, APL Mater. 2019, 7, 031113; g) H. Cho, J. S. Kim, C. Wolf, Y. H. Kim, H. J. Yun, S. H. Jeong, A. Sadhanala, V. Venugopalan, J. W. Choi, C. L. Lee, R. H. Friend, T. W. Lee, ACS Nano 2018, 12, 2883; h) M. Saliba, T. Matsui, J. Y. Seo, K. Domanski, J. P. Correa-Baena, M. K. Nazeeruddin, S. M. Zakeeruddin, W. Tress, A. Abate, A. Hagfeldt, M. Gratzel, Energy Environ. Sci. 2016, 9, 1989; i) P. E. Marchezi, E. M. Therézio, R. Szostak, H. C. Loureiro, K. Bruening, A. Gold-Parker, M. A. Melo, C. J. Tassone, H. C. N. Tolentino, M. F. Toney, A. F. Nogueira, I. Mater. Chem. A 2020, 8, 9302.
- [3] a) M. Hao, Y. Bai, S. Zeiske, L. Ren, J. Liu, Y. Yuan, N. Zarrabi, N. Cheng, M. Ghasemi, P. Chen, M. Lyu, D. He, J.-H. Yun, Y. Du, Y. Wang, S. Ding, A. Armin, P. Meredith, G. Liu, H.-M. Cheng, L. Wang, Nat. Energy 2020, 5, 79; b) D. J. Kubicki, D. Prochowicz, A. Hofstetter, S. M. Zakeeruddin, M. Gratzel, L. Emsley, J. Am. Chem. Soc. 2018, 140, 7232; c) J. Huang, P. Xu, J. Liu, X. Z. You, Small 2017, 13, 1603225.
- [4] a) C. Jia, H. Li, X. Meng, H. Li, Chem. Commun. 2018, 54, 6300;
 b) C. Zhang, S. Wang, X. Li, M. Yuan, L. Turyanska, X. Yang, Adv. Funct. Mater. 2020, 30, 1910582;
 c) G. Jiang, C. Guhrenz, A. Kirch, L. Sonntag, C. Bauer, X. Fan, J. Wang, S. Reineke, N. Gaponik, A. Eychmuller, ACS Nano 2019, 13, 10386;
 d) H. Liu, Y. Tan, M. Cao, H. Hu, L. Wu, X. Yu, L. Wang, B. Sun, Q. Zhang, ACS Nano 2019, 13, 5366;
 e) E. Shi, Y. Gao, B. P. Finkenauer, Akriti, A. H. Coffey, L. Dou, Chem. Soc. Rev. 2018, 47, 6046;
 f) L. Dou, M. Lai, C. S. Kley, Y. Yang, C. G. Bischak, D. Zhang, S. W. Eaton, N. S. Ginsberg, P. Yang, Proc. Natl. Acad. Sci. U. S. A. 2017, 114, 7216.
- [5] a) A. J. Knight, L. M. Herz, Energy Environ. Sci. 2020, 13, 2024;
 b) L. Chen, Y. Y. Tan, Z. X. Chen, T. Wang, S. Hu, Z. A. Nan, L. Q. Xie, Y. Hui, J. X. Huang, C. Zhan, S. H. Wang, J. Z. Zhou, J. W. Yan, B. W. Mao, Z. Q. Tian, J. Am. Chem. Soc. 2019, 141, 1665.
- [6] a) L. Britnell, R. M. Ribeiro, A. Eckmann, R. Jalil, B. D. Belle, A. Mishchenko, Y. J. Kim, R. V. Gorbachev, T. Georgiou, S. V. Morozov, A. N. Grigorenko, A. K. Geim, C. Casiraghi, A. H. Castro Neto, K. S. Novoselov, *Science* 2013, 340, 1311;
 b) E. Shi, B. Yuan, S. B. Shiring, Y. Gao, Akriti, Y. G., C. Su, M. Lai, P. Yang, J. Kong, B. M. Savoie, Y. Yu, L. Dou, *Nature* 2020, 580, 614;
 c) E. Shi, L. Dou, *Acc. Chem. Res.* 2020, 1, 213.
- [7] a) N. T. Shewmon, H. Yu, I. Constantinou, E. Klump, F. So, ACS Appl. Mater. Interfaces 2016, 8, 33273; b) D. Pan, Y. Fu, J. Chen, K. J. Czech, J. C. Wright, S. Jin, Nano Lett. 2018, 18, 1807; c) Y. Wang, Z. Chen, F. Deschler, X. Sun, T. M. Lu, E. A. Wertz, J. M. Hu, J. Shi, ACS Nano 2017, 11, 3355; d) C. S. Liao, Z. L. Yu, P. B. He, B. Liu, R. Zeng, Q. Wan, M. Q. Cai, J. Colloid Interface Sci. 2021, 597, 233; e) Q. Kong, A. Obliger, M. Lai, M. Gao, D. T. Limmer, P. Yang, Nano Lett. 2020, 20, 8151; f) R. M. Kennard, C. J. Dahlman, H. Nakayama, R. A. DeCrescent, J. A. Schuller, R. Seshadri, K. Mukherjee, M. L. Chabinyc, ACS Appl. Mater. Interfaces 2019, 11, 25313.
- [8] a) C. R. Roy, D. Pan, Y. Wang, M. P. Hautzinger, Y. Zhao, J. C. Wright, Z. Zhu, S. Jin, J. Am. Chem. Soc. 2021, 143, 5212; b) Akriti, S. Z.,



www.advmat.de

- Z. Y. Lin, E. Shi, B. P. Finkenauer, Y. Gao, A. J. Pistone, K. Ma, B. M. Savoie, L. Dou, *Adv. Mater.* **2021**, *33*, 2105183.
- [9] A. A. Sutanto, V. I. E. Queloz, I. Garcia-Benito, K. Laasonen, B. Smit, M. K. Nazeeruddin, O. A. Syzgantseva, G. Grancini, APL Mater. 2019, 7, 041110.
- [10] a) A. Amat, E. Mosconi, E. Ronca, C. Quarti, P. Umari, M. K. Nazeeruddin, M. Gratzel, F. De Angelis, *Nano Lett.* 2014, 14, 3608; b) D. J. Kubicki, D. Prochowicz, A. Hofstetter, S. M. Zakeeruddin, M. Gratzel, L. Emsley, J. Am. Chem. Soc. 2017, 139, 14173.
- [11] a) R. B. Little, M. A. El-Sayed, G. W. Bryant, S. Burke, *Chem. Phys.* 2001, 114, 1813; b) Y. Wang, H. Ju, T. Mahmoudi, C. Liu, C. Zhang, S. Wu, Y. Yang, Z. Wang, J. Hu, Y. Cao, F. Guo, Y.-B. Hahn, Y. Mai, *Nano Energy* 2021, 88, 106285.
- [12] a) J. S. Du, D. Shin, T. K. Stanev, C. Musumeci, Z. Xie, Z. Huang, M. Lai, L. Sun, W. Zhou, N. P. Stern, V. P. Dravid, C. A. Mirkin, Sci. Adv. 2020, 6, eabc4959; b) M. Lai, D. Shin, L. Jibril, C. A. Mirkin, J. Am. Chem. Soc. 2022, 144, 13823.
- [13] H. Zhu, M. T. Trinh, J. Wang, Y. Fu, P. P. Joshi, K. Miyata, S. Jin, X. Y. Zhu, Adv. Mater. 2017, 29, 1603072.
- [14] a) Q. Chen, N. De Marco, Y. Yang, T.-B. Song, C.-C. Chen, H. Zhao, Z. Hong, H. Zhou, Y. Yang, Nano Today 2015, 10, 355;
 b) G. R. Berdiyorov, A. Kachmar, F. El-Mellouhi, M. A. Carignano, M. El-Amine Madjet, J. Phys. Chem. C 2016, 120, 16259.
- [15] a) J. Song, J. Li, X. Li, L. Xu, Y. Dong, H. Zeng, Adv. Mater. 2015, 27, 7162; b) M. Ng, J. E. Halpert, RSC Adv. 2020, 10, 3832.
- [16] a) B. Molleman, T. Hiemstra, Phys. Chem. Chem. Phys. 2018,
 20, 20575; b) P. C. Chen, M. Liu, J. S. Du, B. Meckes, S. Wang,
 H. Lin, V. P. Dravid, C. Wolverton, C. A. Mirkin, Science 2019, 363,
 959; c) N. Meethong, H.-Y. S. Huang, W. C. Carter, Y.-M. Chiang,
 Electrochem. Solid-State Lett. 2007, 10, Al34; d) D. Burch,
 M. Z. Bazant, Nano Lett. 2009, 9, 3795.
- [17] a) M. Lai, A. Obliger, D. Lu, C. S. Kley, C. G. Bischak, Q. Kong, T. Lei, L. Dou, N. S. Ginsberg, D. T. Limmer, P. Yang, *Proc. Natl. Acad. Sci. USA* 2018, 115, 11929; b) C. Eames, J. M. Frost, P. R. Barnes, B. C. O'Regan, A. Walsh, M. S. Islam, *Nat. Commun.* 2015, 6, 7497.

- [18] a) A. J. Barker, A. Sadhanala, F. Deschler, M. Gandini, S. P. Senanayak, P. M. Pearce, E. Mosconi, A. J. Pearson, Y. Wu, A. R. Srimath Kandada, T. Leijtens, F. De Angelis, S. E. Dutton, A. Petrozza, R. H. Friend, ACS Energy Lett. 2017, 2, 1416; b) R. E. Beal, D. J. Slotcavage, T. Leijtens, A. R. Bowring, R. A. Belisle, W. H. Nguyen, G. F. Burkhard, E. T. Hoke, M. D. McGehee, J. Phys. Chem. Lett. 2016, 7, 746; c) A. J. Knight, J. Borchert, R. D. J. Oliver, J. B. Patel, P. G. Radaelli, H. J. Snaith, M. B. Johnston, L. M. Herz, ACS Energy Lett. 2021, 6, 799; d) S. Draguta, O. Sharia, S. J. Yoon, M. C. Brennan, Y. V. Morozov, J. S. Manser, P. V. Kamat, W. F. Schneider, M. Kuno, Nat. Commun. 2017, 8, 200.
- [19] E. T. Hoke, D. J. Slotcavage, E. R. Dohner, A. R. Bowring, H. I. Karunadasa, M. D. McGehee, Chem. Sci. 2015, 6, 613.
- [20] a) C. G. Bischak, A. B. Wong, E. Lin, D. T. Limmer, P. Yang, N. S. Ginsberg, J. Phys. Chem. Lett. 2018, 9, 3998; b) W. Mao, C. R. Hall, S. Bernardi, Y. B. Cheng, A. Widmer-Cooper, T. A. Smith, U. Bach, Nat. Mater. 2021, 20, 55.
- [21] a) Z. Xiao, L. Zhao, N. L. Tran, Y. L. Lin, S. H. Silver, R. A. Kerner, N. Yao, A. Kahn, G. D. Scholes, B. P. Rand, Nano Lett. 2017, 17, 6863; b) T. Duong, H. K. Mulmudi, Y. Wu, X. Fu, H. Shen, J. Peng, N. Wu, H. T. Nguyen, D. Macdonald, M. Lockrey, T. P. White, K. Weber, K. Catchpole, ACS Appl. Mater. Interfaces 2017, 9, 26859.
- [22] D. J. Eichelsdoerfer, X. Liao, M. D. Cabezas, W. Morris, B. Radha, K. A. Brown, L. R. Giam, A. B. Braunschweig, C. A. Mirkin, *Nat. Protoc.* 2013, 8, 2548.
- [23] L. Jibril, M. Cheng, C. B. Wahl, V. P. Dravid, C. A. Mirkin, Chem. Mater. 2022, 34, 5094.
- [24] G. Kresse, J. Furthmüller, Phys. Rev. B 1996, 54, 11169.
- [25] a) J. P. Perdew, K. Burke, M. Ernzerhof, Phys. Rev. Lett. 1996, 77, 3865; b) G. Kresse, D. Joubert, Phys. Rev. B 1999, 59, 1758.
- [26] H. J. Monkhorst, J. D. Pack, Phys. Rev. B 1976, 13, 5188.
- [27] a) A. M. Glazer, Phase Transitions 2011, 84, 405; b) A. M. Glazer, Acta Crystallogr., Sect. A: Found. Adv. 1975, 31, 756; c) A. M. Glazer, Acta Crystallogr., Sect. B: Struct. Sci., Cryst. Eng. Mater. 1972, 28, 3384.